Research Article | Vol. 10, No. 12 / 1 December 2019 / Biomedical Optics Express 6625

Biomedical Optics EXPRESS

Multi-plane, wide-field fluorescent microscopy for biodynamic imaging *in vivo*

Ruheng Shi,[1] Cheng Jin,[1] Hao Xie,[2] Yuanlong Zhang,[2] Xinyang Li,[2,3] Qionghai Dai,[2] and Lingjie Kong[1,4,*]

[1] *State Key Laboratory of Precision Measurement Technology and Instruments, Department of Precision Instrument, Tsinghua University, Beijing 100084, China*
[2] *Department of Automation, Tsinghua University, Beijing 100084, China*
[3] *Graduate School at Shenzhen, Tsinghua University, Shenzhen 518055, China*
[4] *IDG/McGovern Institute for Brain Research, Tsinghua University, Beijing 100084, China*
[*] *konglj@tsinghua.edu.cn*

Abstract: Wide-field fluorescent microscopy (WFFM) is widely employed in biomedical studies, due to its inherent advantages in high-speed imaging of biological dynamics noninvasively and specifically. However, WFFM suffers from the loss of axial resolution and the poor resistance to light scattering in deep tissue imaging. Here we propose a novel WFFM which has the capability in optical sectioning and volumetric imaging. We perform speckle illumination with a digital-micromirror-device for optical sectioning and employ an electrically tunable lens for defocusing modulation so as to quickly switch the image planes. We demonstrate its applications in multi-plane, wide-field imaging of biological dynamics in both zebrafish brains and mouse brains *in vivo*.

1. Introduction

Large-scale imaging of biological dynamics, at high spatio-temporal resolutions over extended three-dimensional (3D) volumes, is highly desired in biomedical studies, especially in the study of system biology. Due to its inherent high-speed recording capability and effective cost, wide-field fluorescent microscopy (WFFM) is generally employed [1–3]. However, WFFM suffers from background fluorescence, due to the non-localized excitation and light-scattering induced crosstalk. The background further leads to poor contrast and the loss of optical sectioning capability [4].

So far, several methods have been proposed to achieve wide-field optical sectioning [5–7], except for point scanning based optical sectioning microscopy (such as confocal microscopy and multiphoton microscopy). Neil et al firstly proposed a structured illumination based optical sectioning microscopy (SIM). In this method, three images, recorded at different grid positions with each being laterally translated by a third of the grid period, are computationally combined to calculate an optically sectioned image [7]. However, SIM is highly susceptible to sample motions [8]. To address this problem, HiLo microscopy was proposed ("Hi" and "Lo" for the high and low spatial frequency components, respectively) [8–10]. In HiLo microscopy, only two images were required to achieve optical-sectioning: one for structured-illumination image; the other one for conventional uniform-illumination image. Combining these two images will allow us to recover the optical sectioning image at full frequency bandwidth. Generally, structured illumination can be performed by the interference of coherent light beams [11–12], or by placing a mask, grating or digital-micromirror-device (DMD) on the image plane of the sample [13–16]. Specifically, DMD is a fast, bi-stable spatial light modulator consisting of an array of movable micro-mirrors, where each micro-mirror can be individually rotated ± 12 degree, corresponding to an "on" or "off" state during the illumination.

#375373 https://doi.org/10.1364/BOE.10.006625
Journal © 2019 Received 14 Aug 2019; revised 5 Oct 2019; accepted 30 Oct 2019; published 27 Nov 2019

Biomedical Optics EXPRESS

Once one achieves optical sectioning, multi-plane imaging is possible. To record biological dynamics over extended three-dimensional volumes in optical-sectioning imaging, fast axial scanning should also be performed. Conventionally, axial scanning is achieved by mechanical moving the objectives or the biological samples, whose maximal speed would suffer from the inertia. Recently, an axial scanning method based on the electrically tunable lenses (ETL) was proposed. Modulating defocusing with the ETL enables fast axial scanning with no perturbation of the samples, and thus allows high-speed volumetric imaging. Recently, a variety of point-scanning microscopy techniques, such as confocal microscopy [17,18] and two photon microscopy [19], have integrated ETL for multi-plane imaging. For wide-field imaging of optical-sectioning capability, such as SIM [20], adopting an ETL would also enable 3D imaging without mechanical scanning. However, no HiLo microscopy integrated with ETL for *in vivo* high-speed volumetric imaging has been demonstrated yet.

Here we propose a new multi-plane, wide-field fluorescence microscopy for recording biodynamics *in vivo*, based on speckle illumination for optical sectioning and defocusing modulation for volumetric imaging. We employ a DMD, which is conjugated to the sample plane, as a speckle generator, and an ETL for defocusing modulation which enables rapid switching of focal planes. To demonstrate the superior performance of our technique, we first calibrate the optical resolution and field-of-view (FOV), then apply it in multi-plane, wide-field imaging of vascular dilations and neural network activity *in vivo*.

2. The optical sectioning in HiLo microscopy

The basics of HiLo microscopy was described in detail by Lim and Mertz [8–10], which is based on the "double-acquisition" mode. A uniformly illuminated image is used to extract the in-focus high-frequency components, and a speckle-illuminated image is used to extract the in-focus low-frequency components. The corresponding intensity distributions of the uniformly illuminated and speckle images are denoted as $I_u(\vec{\rho})$ and $I_s(\vec{\rho})$, respectively. The intensity distributions of the in-focus high- and low- frequency images are referred as $I_{Lo}(\vec{\rho})$, $I_{Hi}(\vec{\rho})$, with the 2D spatial coordinate $\vec{\rho}$. The high-frequency components attenuate more rapidly than the lower-frequency components with the increasing of the defocus range [21]. Thus, we can get the in-focus high-frequency components by applying the high-pass filter on the uniformly-illuminated image:

$$I_{Hi}(\overrightarrow{\rho}) = HP[I_u(\overrightarrow{\rho})] \tag{1}$$

whereby HP denotes a Gaussian high-pass filter with the cutoff frequency Kc applied in the frequency domain.

To obtain the in-focus low-frequency components, we need to estimate the contrast of speckle-illuminated image:

$$C_s(\overrightarrow{\rho}) = \sigma[I_s(\overrightarrow{\rho})] \tag{2}$$

where σ is the standard deviation of the imaged fluorescence variations.

In practice, mostly samples are non-uniform. The overall spatial contrast $C_s(\vec{\rho})$ is both influenced by the speckle pattern in the illumination and the sample-induced noise. We can use the difference image:

$$I_d(\overrightarrow{\rho}) = I_u(\overrightarrow{\rho}) - I_s(\overrightarrow{\rho}) \tag{3}$$

for contrast calculation. Through this way, the contrast induced by the non-uniform sample can be removed.

Biomedical Optics EXPRESS

Now we can estimate the illumination induced contrast by:

$$C(\overrightarrow{\rho}) = \sigma[I_d(\overrightarrow{\rho})] \tag{4}$$

Furthermore, we can apply a band-pass filter:

$$BP(\overrightarrow{k}) = \exp(-\frac{|k^2|}{2\sigma_s^2}) - \exp(-\frac{|k^2|}{\sigma_s^2}) \tag{5}$$

on the difference image to increase the axial resolution [10] before evaluating the C($\vec{\rho}$). The in-focus low-frequency components are then constructed by applying a low-pass filter (LP) to the weighted uniformly-illuminated image, obtaining:

$$I_{Lo}(\overrightarrow{\rho}) = LP[C(\overrightarrow{\rho})I_u(\overrightarrow{\rho})] \tag{6}$$

By adjusting the width of this band-pass filter, we can tune the optical sectioning strength of low-frequency components. In order to adjust the optical sectioning strength of the high-frequency components, the cut-off frequency of the Gaussian high-pass filter is tuned by setting $Kc = 0.18$ δ_s [10], based on the Stokseth approximation [22] of 3D optical-transfer-function in wide-field microscope.

The final optical-sectioning image is synthesized from the fusion of the above two images, resulting in:

$$I_{HiLo}(\overrightarrow{\rho}) = I_{Hi}(\overrightarrow{\rho}) + \eta I_{Lo}(\overrightarrow{\rho}) \tag{7}$$

where η is a scaling factor that ensures a seamless transition at full frequency bandwidth.

3. Experimental setup and system calibration

The diagram of the experimental setup is shown in Fig. 1(a). We use a LED light (120LED, X-Cite) as the illumination source. In this experiment, we use a speckle image to extract the in-focus low-frequency components. Speckle is generated by displaying a random binary pattern onto a DMD (DLP9500, TI), from which a uniform illumination can also be achieved by presenting a flat mirror pattern. To make the system compact, we employ a total internal reflection (TIR) prism to separate the illumination and projection paths [23]. After TIR, the generated non-uniform or uniform light passes through the two sets of relay: one consists of L1 (AC508-100-A, Thorlabs) and L2 (AC508-300-A, Thorlabs); the other one consists of L3 (AC508-180-A, Thorlabs) and "ETL-objective" set. By placing the tunable lens in a plane conjugate to the back pupil plane, the system can maintain constant magnification and resolution in the process of adjusting ETL. Since the back pupil is mostly inside of the objective, to access the back-pupil plane, one needs to relay the back pupil plane out. To simplify the system, we directly place the ETL (EL-C-10-30-VIS-LD, Optotune AG, Switzerland) before the objective, as in [24]. The aperture diameter of ETL is 10 mm. In order to avoid light blocking by the objective, the aperture size of the objective and ETL must match. Thus we choose the CFI Plan Fluor 20×/0.5 (Nikon) objective and the XLPLN25XWMP2, 25×/1.05 (Olympus) objective, both with the aperture diameter of 10 mm. The former one is used for system calibration and investigating the vascular dilations in mouse cerebral cortex *in vivo*. The latter one is used for calcium imaging of zebrafish brain *in vivo*, which ensures a higher fluorescence collection efficiency.

In order to maintain a large FOV, instead of using standard f = 200 mm tube lens, we use L4 (f = 100 mm, AC508-100-A, Thorlabs) as the tube lens. In theory, the 20× objective is working at 10× magnification (~ 9× through experimental calibration). A sCMOS camera (2160×2560 pixels, pixel size: 6.5 µm, Zyla 5.5 sCMOS, Oxford Instruments) is used for image recording.

According to Rayleigh criterion, the laterally optical resolution is 628 nm (λ_{ex} = 515 nm, NA = 0.5). Since the objective is working at 9× magnification, the size of each pixel (6.5 µm)

Biomedical Optics EXPRESS

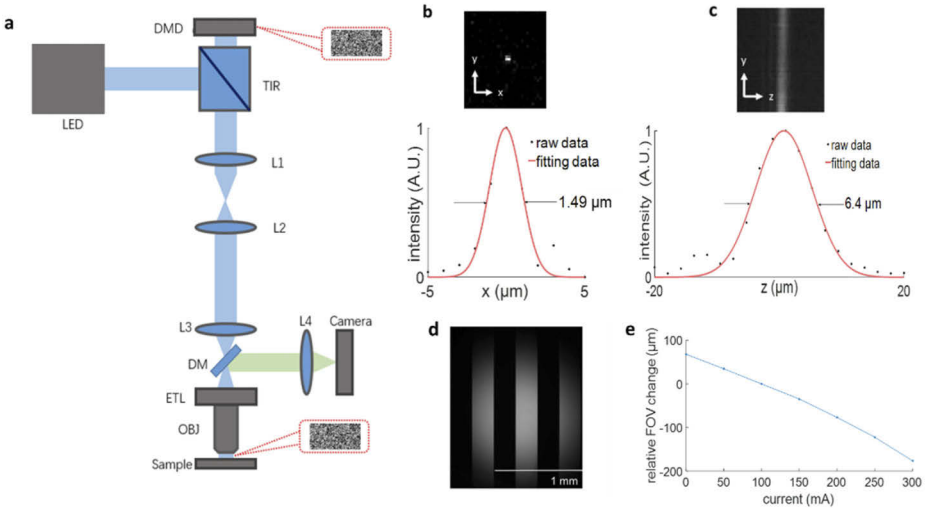

Fig. 1. Optical setup and the calibration results. (a) Experimental setup. The light from a light-emitting-diode (LED) is delivered to the digital-micromirror-device (DMD) with a total internal reflection prism (TIR). The binary pattern on the DMD is projected onto the sample plane through two sets of relay lenses, one consists of L1 (f = 100 mm) and L2 (f = 300 mm); the other one consists of L3 (f = 180 mm) and "electrically tunable lens (ETL)-objective (OBJ)" set. Fluorescence signals from the specimen is collected by the objective, reflected by the dichroic mirror (DM), and imaged onto the sCMOS camera by L4 (f = 100 mm). (b) Lateral point-spread function (PSF) determined with 0.5 μm fluorescent beads. The measured FWHM is 1.49 μm. (c) Axial PSF determined with a fluorescent sheet. The measured FWHM is 6.4 μm. (d) Field-of-view measured from a specific test target: 1.56 mm × 1.83 mm. (e) The relative field-of-view change versus the applied current.

corresponds to 0.72 μm at the sample plane. According to Nyquist sampling theorem, the camera limited lateral resolution is 1.44 μm. To calibrate the lateral resolution experimentally, we use sub-resolution fluorescent beads (0.5 μm) as the sample. The lateral full-width-at-half-maximum (FWHM) is 1.49 μm (fitted to a Gaussian function, Fig. 1(b)), suggesting that the lateral resolution of our system is mainly limited by the pixel size of the imaging sensor.

The optical-sectioning capability of HiLo microscopy can be calculated as:

$$FWHM_{\text{axial}} = \frac{0.54}{K_S \times NA} \tag{8}$$

where K_s=1/(2 Δ_s), Δ_s is the size of speckle grains on the sample plane [25]. Since the FWHM of lateral PSF determined with the sub-resolution beads is 1.49 μm, the smallest size of the speckle grains we can choose is 1.49 μm, which corresponds to the axial resolution of 3.2 μm. Even though larger speckle grains correspond to higher contrast, considering the fluorescence background is very intense, the speckle size we choose is 2.98 μm. This speckle size corresponds to axial resolution of 6.4 μm. To test the optical-sectioning capability of our microscopy experimentally, image stacks of FITC layers are recorded. Fluorescence intensity is averaged over the whole FOV and plotted along z positions. In Fig. 1(c), raw data are displayed as black dots, and fitting data are displayed in red line, from which the axial FWHM is 6.4 μm (fitted to a Gaussian function), same as the FHWM calculated from Eq. (8). Considering that the size of each neural soma is ~10 μm [26], we expect that, our system would be able to image cellular or even subcellular structures.

Biomedical Optics EXPRESS

To measure the FOV of our system, we use a resolution test target (R2L2S1P1, Thorlabs) as the ground truth. The frequency of the specific test target is 2 cycles/mm, thus the diameter of the measured FOV is 1.83 mm. Considering the size of the sCMOS camera used in our setup, we can record biodynamics in the range of 1.56 mm×1.83 mm (Fig. 1(d)). By adjusting the current of the ETL to focus at different depths, we measure the relative FOV diameter displacement and find that it varies from 67.87 μm to −176.5 μm (Fig. 1(e)). This suggests that we can observe large-scale dynamics at different planes with stable FOVs, and the lateral shift will not affect the registration of features between different planes apparently.

Moreover, we calibrate the axial displacements versus applied currents. We use 3 μm fluorescent beads diluted in 1% agarose as the specimen. Due to the stretching of the axial PSF, there is about 3 μm errors when we perform focusing. We could further reduce the error by using smaller beads. In order to obtain the displacement of focus position, we firstly move the beads into sharp focusing through driving the motorized stage, then change the applying current, followed by re-focusing the beads through moving the motorized stage. The result is depicted in Fig. 2(a). The axial position of focal plane varies from 204 μm to −494 μm, thus a total defocus range of 698 μm is covered. According to Fig. 2(a), the axial displacement function shows hysteresis behavior. However, this phenomenon will not affect multi-plane imaging, as observed in following experiments.

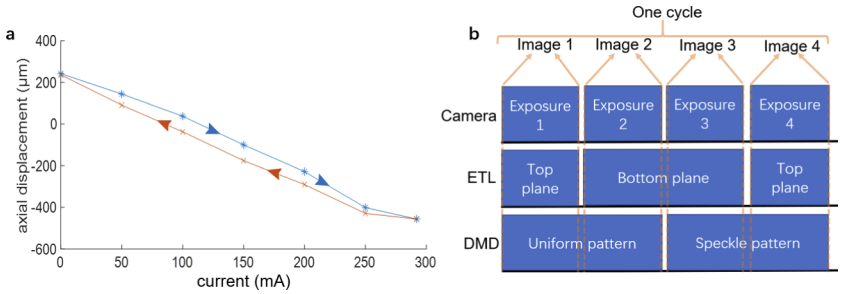

Fig. 2. The calibration of axial positions at specific currents of ETL and the signal synchronization for image acquisition. (a) The axial displacement versus applied current of the ETL. The blue arrow indicates the direction of rising current (from 0 to 292 mA), and the yellow arrow indicates the direction of decreasing current (from 292 to 0 mA). (b) The signal synchronization for image acquisition.

To perform multi-plane, optical-sectioning imaging, we synchronize the DMD, ETL, and camera with a data acquisition card (USB-6363, National Instruments Corporation). Both the DMD and the camera are trigged by the rising edge of the control signal. The DMD alternates the patterns for uniform illumination and speckle illumination when a rising edge comes, and the camera starts an exposure event when a rising edge comes. For ETL, the input control voltage varies from 0 to 5 V, corresponding to the preset minimum axial position and preset maximum axial position, respectively. For example, in dual-plane imaging, we divide one cycle into the acquisition of four images, as describes in Fig. 2(b). Image 1 and 2 represent the uniformly-illuminated images at the top plane and the bottom plane, respectively. Image 3 and 4 represent the speckle-illuminated images at bottom plane and the top plane, respectively. Similarly, we can perform three-plane imaging and so on.

4. Experimental results

All procedures involving animals were approved by the Animal Care and Use Committees of Tsinghua University.

Biomedical Optics EXPRESS

4.1. Dual-plane imaging of vascular dilations in mouse cerebral cortex in vivo

To demonstrate the advantages of our system in large-scale imaging of biodynamics at high spatio-temporal resolution, we firstly perform dual-plane imaging of vascular dilations in mouse cerebral cortex *in vivo*. We use adult C57BL/6 mice and perform craniotomy for chronic imaging. After one month, we inject FITC (70,000 MW, Sigma Aldrich) into the blood vessels [27] (2% w/v in saline, 200 mg/ kg) for staining the blood plasma, an indirect way to label the vascular system, when the mice are under anesthesia. The imaging is performed when the mice are awake and head-restrained under the microscope objective.

Using the synchronization strategy mentioned above, we perform alternate dual-plane imaging of FITC-stained blood vessels at 5 Hz (Fig. 3, Visualization 1). The axial interval between the two plane is 45 μm. In Fig. 3(a) and Fig. 3(c), we show the uniformly-illuminated images of the top plane and the bottom plane, respectively, as acquired with conventional WFFM. In Fig. 3(b) and Fig. 3(d), we show the corresponding optical-sectioning images, acquired in the HiLo mode. The vessel marked with green arrows (Fig. 3(a)–(d)) is maintained in-focus at the top plane (Fig. 3(a) and (b)), while is out-of-focus at the bottom plane (Fig. 3(c) and (d)). The out-of-focus vessel shows as blurred information in the uniformly-illuminated image (Fig. 3(c)), which diminishes contrast largely. Using our optical-sectioning method, this blurred information is removed (Fig. 3(d)). It suggests that our method can get rid of out-of-focus information while keeping in-focus information.

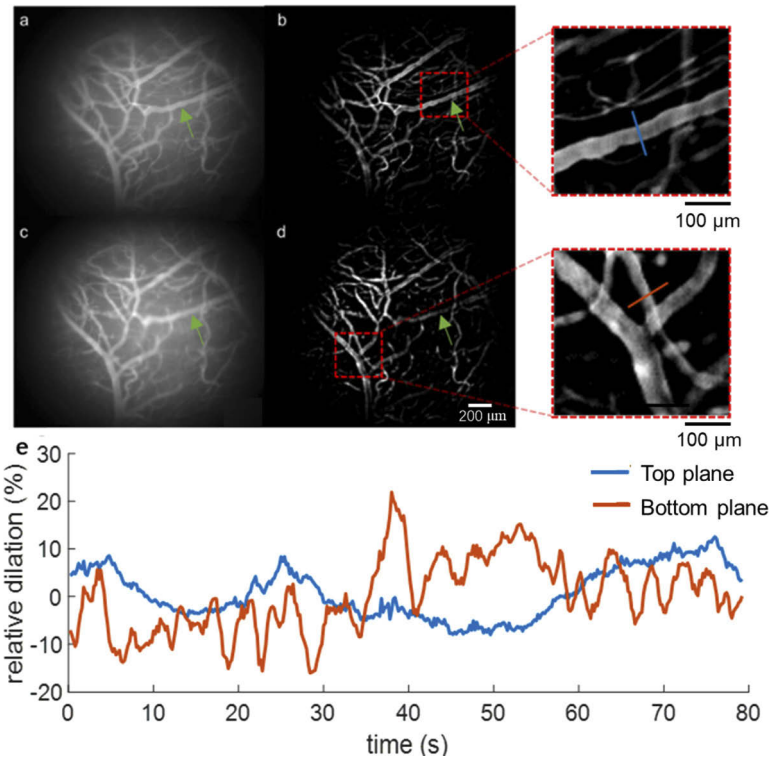

Fig. 3. Dual-plane imaging of vascular dilations in mouse cerebral cortex *in vivo*. (a, b) Uniformly-illuminated image and optical-sectioning image of the top plane, respectively. (c, d) Uniformly-illuminated image and optical-sectioning image of the bottom plane (45 μm deeper), respectively. The insert shows the detail spatial morphology of blood vessels. (e) Dilations relative to the average diameters of blood vessels at the top and bottom planes (see also Visualization 1).

Biomedical Optics EXPRESS

Besides, we can observe the dilations of blood vessels [28,29] at both the top plane (red curves) and the bottom plane (blue curves) alternately (Fig. 3(e)), whose region-of-interests (ROIs) are shown in the red-dashed box of Fig. 3(b) and Fig. 3(d), respectively. The capability in large-scale volumetric imaging of vascular dilations provides a potential means to study neurovascular coupling *in vivo*.

4.2. Three-plane calcium imaging of Zebrafish brain in vivo

To demonstrate the capacity of our system in functional imaging *in vivo*, we perform calcium imaging in zebrafish brains. We use Tg (HUC:H2B-GCaMP6f) zebrafish at 5–7 days' post fertilization. To fix the zebrafish larvae, we embed them in 1% agarose.

We perform three-plane imaging of calcium dynamics in the HiLo mode in awake zebrafishes expressing GCaMP6f (Fig. 4, Visualization 2). In order to ensure decent signal-to-noise ratio, we set the exposure time for each acquisition event as 100 ms, corresponding to a frame rate of 1.6 Hz limited by the illumination power. As expected, conventional uniformly-illuminated images [Fig. 4(a), Fig. 4(c) and Fig. 4(e)] suffer from background fluorescence, whereas optical-sectioning imaging achieve images of much higher contrast (Fig. 4(b), Fig. 4(d) and Fig. 4(f)).

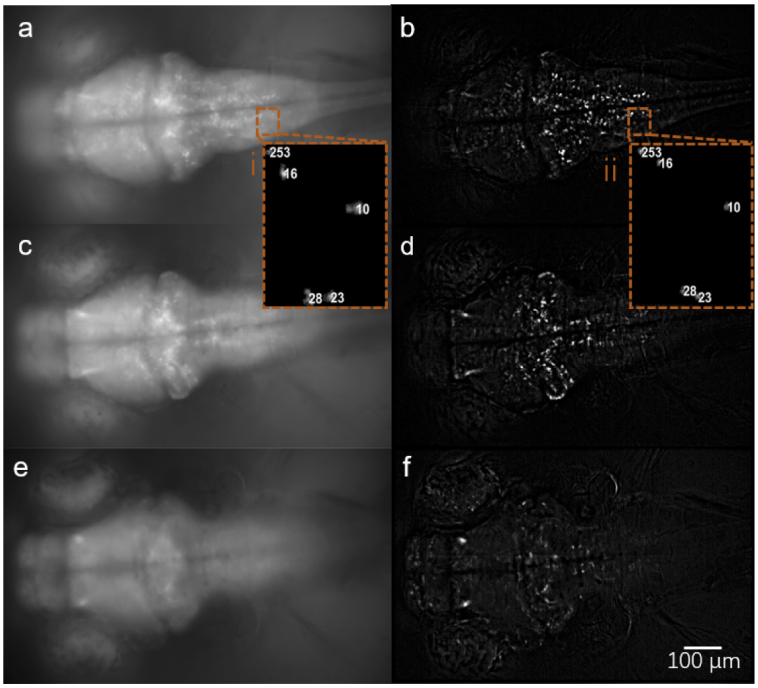

Fig. 4. Three-plane calcium imaging of zebrafish brain *in vivo*. (a, c, and e) Uniformly-illuminated images of the top, middle, and bottom planes, respectively. (b, d, and f) Optical-sectioning images of the corresponding planes as in a, c, and e. The inserts in (a) and (b) show the ROI in the top plane for further discussion in Fig. 5. The axial scanning range is 105 μm, with the interval between each plane being 52.5 μm (see also Visualization 2).

To trace calcium signals of single neurons, we firstly perform motion correction, then extract calcium signals based on the extended constrained non-negative matrix factorization method [30]. To show the optical sectioning capability and its robustness to scattering-induced cross-talk in calcium imaging, we compare fluorescence variations ($\Delta F/F$) of the calcium indicator measured from selected ROIs in the uniformly-illuminated (insert i in Fig. 4(a)) and HiLo (insert ii in Fig. 4(b)) modes [31]. Considering that the raw $\Delta F/F$ in uniformly-illuminated mode is too

Biomedical Optics EXPRESS

low, we enlarge it by a factor of 5 (Fig. 5(a), black curve). Figure 5 shows the increased $\Delta F/F$ amplitudes in the HiLo mode, where HiLo mode leads to a gain of $\Delta F/F$ by a factor of more than 5 compared to that in conventional uniformly-illuminated microscopy. The much lower $\Delta F/F$ in uniformly-illuminated mode indicates that out-of-focus fluorescence contributes to the baseline fluorescence intensity (F) and lowers the amplitude of $\Delta F/F$ from single neurons. Moreover, it should be noted that there are fluorescence peaks which show up in the uniformly-illuminated mode but not in the HiLo mode (pointed out by arrows in Fig. 5(a) as examples), suggesting that background fluorescence in uniformly-illuminated mode may introduce artifacts.

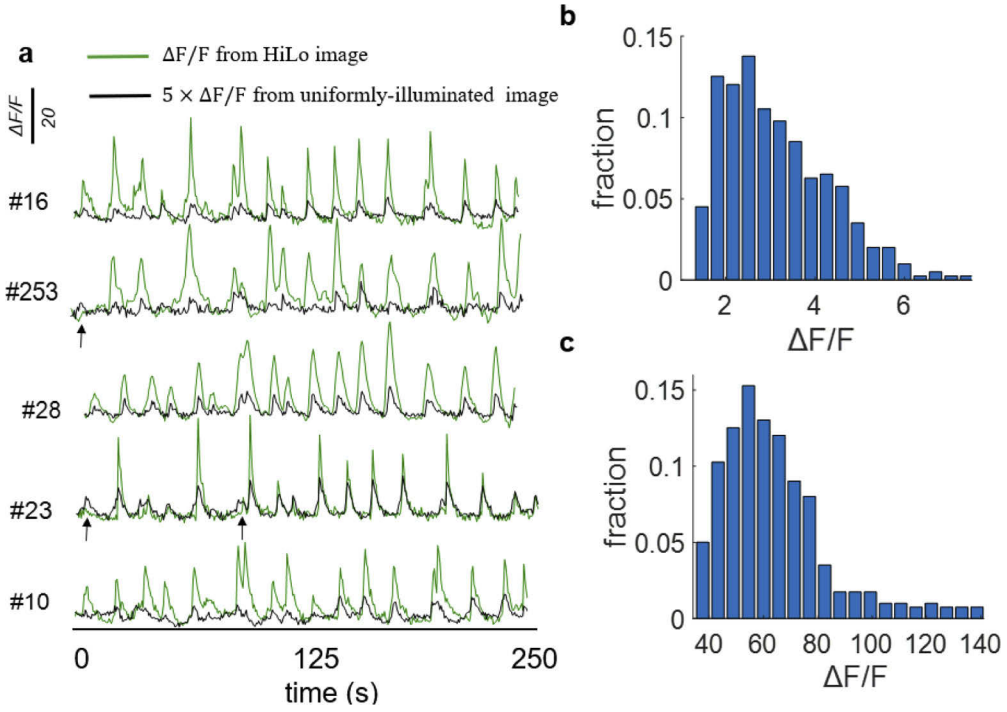

Fig. 5. Calcium tracing of neurons recorded in the uniformly-illuminated and optical-sectioning modes, at the top plane. (a) Fluorescent intensity dynamics in both modes, with the ROIs labeled in the inserts of Fig. 4 (a) and (b). The calcium tracing intensities of uniformly-illuminated mode are enlarged by a factor of 5. Arrows indicate the artifacts introduced by background fluorescence in the uniformly-illuminated mode. (b, c) The histogram of the $\Delta F/F$ in the uniformly-illuminated and HiLo modes, respectively, at the top plane.

We further investigate the distribution of maximal fluorescence variation [31] in the HiLo and uniformly-illuminated modes of the whole top plane. The median number of calcium transients in individual neurons of uniformly-illuminated mode is 2.9886, which is much smaller than the value from the images obtained with HiLo mode (48.1463). Such a boost of fluorescence variation detection reveals higher sensitivity of HiLo mode in identifying neural activity with respect to that in the conventional observation.

In Fig. 6, we extract the calcium signal of HiLo images in all three planes. Fluorescence dynamics of ~900 neurons are detected, and the estimated contours of each plane are shown in Fig. 6(a-c). We present the calcium tracings of each plane in Fig. 6(d), Fig. 6(e) and Fig. 6(f). The zoom-in view of calcium signals from 40 example neurons at each plane are shown in Fig. 6(h).

Biomedical Optics EXPRESS

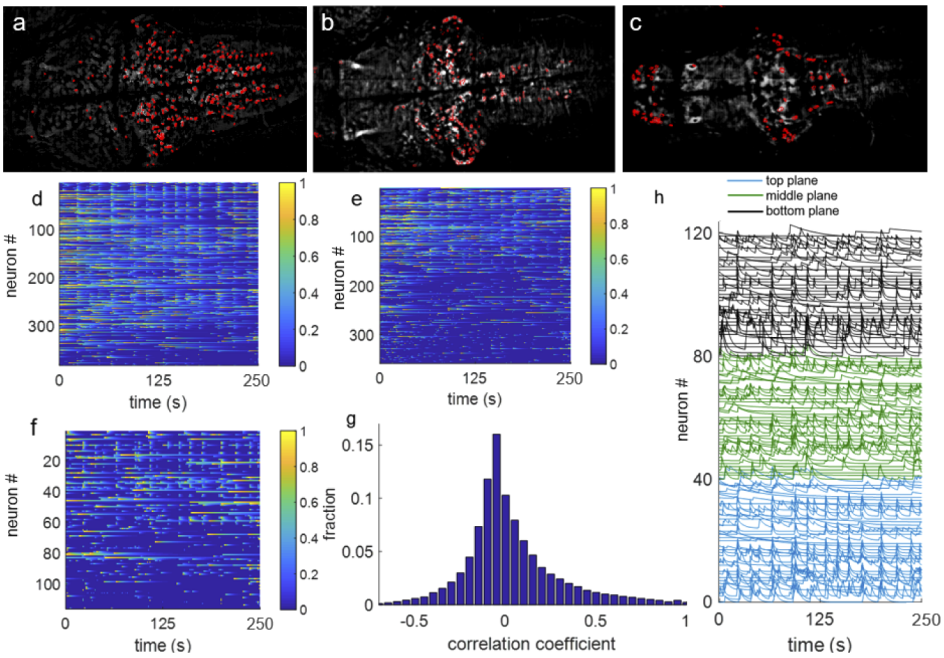

Fig. 6. Calcium tracing of single neurons from HiLo images. (a-c) Estimated neuron contours at the top, middle, and bottom planes of the optical-sectioning images. (d-f) Calcium traces of single neurons at the top, middle, and bottom planes. (g) The histogram of the correlation coefficients. (h) Calcium signals from 40 example neurons at each plane.

Furthermore, we investigate the correlations between pairs of neurons to study whether the $\Delta F/F$ detected from each neuron reflected its own activity or is overwhelmed by the background [32]. If the $\Delta F/F$ detected from individual neurons mostly reflects the change in out-of-focus fluorescence, correlations between pairs of neurons would be high. We therefore compute the pair-wise correlation coefficients for the calcium traces between each pair of neurons, as shown in Fig. 6(g). According to the distribution, more than 60% of correlation coefficients are < 0.2. This indicates that most correlations between pairs of neurons show weak correlation, which further means the $\Delta F/F$ detected from each neuron is not overwhelmed by the background fluorescence.

5. Conclusions

We propose a new multi-plane WFFM, capable of optical sectioning and volumetric imaging. Based on the calibration results, we achieve axial optical sectioning of 6.4 μm, lateral resolution of 1.49 μm over the FOV of 1.56 mm × 1.83 mm. To ensure a large FOV, the lateral resolution is limited by under-sampling in current setup, but it's acceptable considering the size of neural soma is ~10 μm.

Furthermore, we perform multiplane imaging of biodynamics *in vivo* to demonstrate the superior performance of our system. We image the dilations of FITC-stained blood vessels at different depths in mouse brains, and perform *in vivo* calcium imaging of zebrafish brains at three different depths. The results show that our proposed method is more sensitive, and can get rid of background fluorescence which may introduce artifacts as in conventional WFFM.

The highest frame rate we demonstrated is 5 Hz for dual-plane imaging of vascular dilations. To achieve a higher frame rate, one can employ a higher NA objective to improve the fluorescence collection efficiency, or properly increase the power of illumination light. In practice, the

Biomedical Optics EXPRESS

photodamage induced by too much excitation power is another concern. Considering the response time of ETL is ~10 ms and the valid exposure time for each image is ~ 40 ms, we can further reduce the exposure time by increasing the power of illumination light under a safe threshold.

We expect that our technique would find wide applications in 3D, biodynamic imaging *in vivo*.

Funding

National Natural Science Foundation of China (61831014, 61771287); Graduate Education Innovation Grants, Tsinghua University.

Acknowledgment

RS thanks Zheng Jiang for helps in zebrafish preparation. LK thanks the support from Tsinghua University and the "Thousand Talents Plan" Youth Program.

Disclosures

The authors declare that there are no conflicts of interest related to this article.

References

1. H. R. Maricq, "Wide-field capillary microscopy," Arthritis Rheum. **24**(9), 1159–1165 (1981).
2. M. Böhmer and J. Enderlein, "Orientation imaging of single molecules by wide-field epifluorescence microscopy," J. Opt. Soc. Am. B **20**(3), 554–559 (2003).
3. J. R. Swedlow and M. Platani, "Live Cell Imaging Using Wide-Field Microscopy and Deconvolution," Cell Struct. Funct. **27**(5), 335–341 (2002).
4. J. Mertz, "Optical sectioning microscopy with planar or structured illumination," Nat. Methods **8**(10), 811–819 (2011).
5. P. A. Santi, "Light Sheet Fluorescence Microscopy: A Review," J. Histochem. Cytochem. **59**(2), 129–138 (2011).
6. Verveer, Hanley, Verbeek, van Vliet, and Jovin, "Theory of confocal fluorescence imaging in the programmable array microscope (PAM)," J. Microsc. **189**(3), 192–198 (1998).
7. M. A. A. Neil, R. Juškaitis, and T. Wilson, "Method of obtaining optical sectioning by using structured light in a conventional microscope," Opt. Lett. **22**(24), 1905–1907 (1997).
8. S. Santos, K. K. Chu, D. Lim, N. Bozinovic, T. N. Ford, C. Hourtoule, A. C. Bartoo, S. K. Singh, and J. Mertz, "Optically sectioned fluorescence endomicroscopy with hybrid-illumination imaging through a flexible fiber bundle," J. Biomed. Opt. **14**(3), 030502 (2009).
9. N. Bozinovic, C. Ventalon, T. Ford, and J. Mertz, "Fluorescence endomicroscopy with structured illumination," Opt. Express **16**(11), 8016–8025 (2008).
10. D. Lim, T. N. Ford, K. K. Chu, and J. Mertz, "Optically sectioned in vivo imaging with speckle illumination HiLo microscopy," J. Biomed. Opt. **16**(1), 016014 (2011).
11. M. A. A. Neil, R. Juškaitis, and T. Wilson, "Real time 3D fluorescence microscopy by two beam interference illumination," Opt. Commun. **153**(1–3), 1–4 (1998).
12. J. T. Frohn, H. F. Knapp, and A. Stemmer, "True optical resolution beyond the Rayleigh limit achieved by standing wave illumination," Proc. Natl. Acad. Sci. U. S. A. **97**(13), 7232–7236 (2000).
13. M. G. Gustafsson, "Surpassing the lateral resolution limit by a factor of two using structured illumination microscopy," J. Microsc. **198**(2), 82–87 (2000).
14. M. A. Neil, A. Squire, R. Juskaitis, P. I. Bastiaens, and T. Wilson, "Wide-field optically sectioning fluorescence microscopy with laser illumination," J. Microsc. **197**(1), 1–4 (2000).
15. D. Dudley, W. M. Duncan, and J. Slaughter, "Emerging digital micromirror device (DMD) applications," Proc. SPIE **4985**, 14 (2003).
16. D. H. Kim, J. Kim, J. C. Marques, A. Grama, D. G. C. Hildebrand, W. Gu, J. M. Li, and D. N. Robson, "Pan-neuronal calcium imaging with cellular resolution in freely swimming zebrafish," Nat. Methods **14**(11), 1107–1114 (2017).
17. M. Duocastella, G. Vicidomini, and A. Diaspro, "Simultaneous multiplane confocal microscopy using acoustic tunable lenses," Opt. Express **22**(16), 19293–19301 (2014).
18. S. A. Khan and N. A. Riza, "Demonstration of a no-moving-parts axial scanning confocal microscope using liquid crystal optics," Opt. Commun. **265**(2), 461–467 (2006).
19. W. Yang, L. Carrillo-Reid, Y. Bando, D. S. Peterka, and R. Yuste, "Simultaneous two-photon imaging and two-photon optogenetics of cortical circuits in three dimensions," eLife **7**, e32671 (2018).
20. T. Hinsdale, B. H. Malik, C. Olsovsky, J. A. Jo, and K. C. Maitland, "Volumetric structured illumination microscopy enabled by a tunable-focus lens," Opt. Lett. **40**(21), 4943–4946 (2015).
21. D. Dan, B. Yao, and L. J. S. B. Ming, "Structured illumination microscopy for super-resolution and optical sectioning," Sci. Bull. **59**(12), 1291–1307 (2014).

Biomedical Optics EXPRESS

22. P. Stokseth, "Properties of a defocused optical system," J. Opt. **59**(10), 1314–1321 (1969).
23. D. Dan, M. Lei, B. Yao, W. Wang, M. Winterhalder, A. Zumbusch, Y. Qi, L. Xia, S. Yan, Y. Yang, P. Gao, T. Ye, and W. Zhao, "DMD-based LED-illumination super-resolution and optical sectioning microscopy," Sci. Rep. **3**(1), 1116 (2013).
24. B. F. Grewe, F. F. Voigt, M. V. Hoff, and F. Helmchen, "Fast two-layer two-photon imaging of neuronal cell populations using an electrically tunable lens," Biomed. Opt. Express **2**(7), 2035–2046 (2011).
25. T. N. Ford, D. Lim, and J. Mertz, "Fast optically sectioned fluorescence HiLo endomicroscopy," J. Biomed. Opt. **17**(2), 021105 (2012).
26. D. W. Zaidel, M. M. Esiri, and P. J. Harrison, "Size, shape, and orientation of neurons in the left and right hippocampus: investigation of normal asymmetries and alterations in schizophrenia," Am. J. Psychiatry **154**(6), 812–818 (1997).
27. A. Florence, G. Sabine, B. Sylvie, R. M. Johannes, V. Jean-Claude, A. Mireille, M. Mathieu, D. Antoine, G. Isabelle, and V. D. S. Boudewijn, "Specific in vivo staining of astrocytes in the whole brain after intravenous injection of sulforhodamine dyes," PLoS One **7**(4), e35169 (2012).
28. J. H. Park, L. Kong, Y. Zhou, and M. Cui, "Large-field-of-view imaging by multi-pupil adaptive optics," Nat. Methods **14**(6), 581–583 (2017).
29. J. Fan, J. Suo, J. Wu, H. Xie, Y. Shen, F. Chen, G. Wang, L. Cao, G. Jin, Q. He, T. Li, G. Luan, L. Kong, Z. Zheng, and Q. Dai, "Video-rate imaging of biological dynamics at centimetre scale and micrometre resolution," Nat. Photonics **13**, 809–816 (2019).
30. P. Zhou, S. L. Resendez, J. Rodriguez-Romaguera, J. C. Jimenez, S. Q. Neufeld, A. Giovannucci, J. Friedrich, E. A. Pnevmatikakis, G. D. Stuber, R. Hen, M. A. Kheirbek, B. L. Sabatini, R. E. Kass, and L. Paninski, "Efficient and accurate extraction of in vivo calcium signals from microendoscopic video data," eLife **7**, e28728 (2018).
31. M. A. Lauterbach, E. Ronzitti, J. R. Sternberg, C. Wyart, and V. Emiliani, "Fast Calcium Imaging with Optical Sectioning via HiLo Microscopy," PLoS One **10**(12), e0143681 (2015).
32. E. Yoshida, S.-I. Terada, Y. H. Tanaka, K. Kobayashi, M. Ohkura, J. Nakai, and M. Matsuzaki, "In vivo wide-field calcium imaging of mouse thalamocortical synapses with an 8 K ultra-high-definition camera," Sci. Rep. **8**(1), 8324 (2018).